Integration of SRTM and ASTER data for litho-structural and alteration mapping in Nholi area, central Tanzania

Muhudi Ngerezi, Nureddin Saadi, Akira Imai, Waleed Ibrahim*

Abstract. In this study, satellite imagery was used for structural and alteration mapping in the Nholi area, central Tanzania. Structural mapping was carried out by processing and interpreting SRTM-DEM data using remote sensing and GIS techniques. Various band ratios and the Relative Absorption Band Depth (RBD) method of ASTER image were used to delineate hydrothermal alteration zones. The orientation analysis of the extracted lineaments indicates that the study area is controlled by five structural trends: NE–SW, WNW–ESE, N–S, E–W and NW–SE. The VNIR and SWIR bands of ASTER data were effective in delineating hydrothermal alteration mineral zones associated with gold mineralization. The spatial distribution of hydrothermal alteration zones was verified by field survey, microscopic studies and XRD analysis. Furthermore, the extension of alteration zones around the known gold deposit together with lineaments has led to the identification of new potential areas. Data integration shows a positive correlation between the extracted lineaments and hydrothermal alteration zones, which may indicate that the mineralization in the study area is structurally controlled. Moreover, the microscopic study of sulphide minerals revealed both syn- and post-shearing characteristics.

Keywords: structural mapping; hydrothermal alteration; band ratios; lineaments analysis; mineralization

✉ *Muhudi Ngerezi (muhidini.ngerezi@gst.go.tz),* ⓘ *https://orcid.org/0009-0005-8288-8975;*
Geological Survey of Tanzania, Dodoma, Tanzania;

Nureddin Saadi* (n.saadi@uot.edu.ly), ⓘ *https://orcid.org/0000-0003-0593-8578;*
Department of Geological Engineering, Faculty of Engineering, University of Tripoli, Libya;

Akira Imai (imai@mine.kyushu-u.ac.jp), ⓘ *https://orcid.org/0000-0002-3058-9915;*
Department of Earth Resources Engineering, Kyushu University, Fukuoka, Japan;

Waleed Ibrahim (dr.waleedelghazalawi@yahoo.com); ⓘ *https://orcid.org/0000-0001-5725-0535;*
Nuclear Materials Authority, Cairo, Egypt

INTRODUCTION

Surface mineralogy mapping using remote sensing techniques offers great opportunities for more efficient mineral exploration (Peyghambari, Zhang 2021; Mars, Rowan 2006). Remote sensing approaches have become attractive for the detection of hydrothermal alteration minerals because they are fast and require little labour (Pour, Hashim 2014; Pournamdari *et al*. 2014). Advanced satellite imagery is used by exploration geologists to identify and map hydrothermal alteration zones for prospecting gold deposits during the reconnaissance phases (Gabr *et al*. 2010; Liu *et al*. 2017). The multi-temporal satellite images with enhanced spatial and spectral resolutions are highly efficient in mapping alteration zones for gold exploration (Mbianya *et al*. 2021). The current use of remote sensing techniques in gold deposit exploration is indirect, through delineating the hydrothermal alteration zones that are likely to be associated with ore deposits (Testa *et al*. 2018). Certain diagnostic groups of hydrothermal minerals, such as clays, phyllosilicates, carbonates and sulphates, can be identified based on their spectral signatures with diagnostic

features in the Short-Wave Infrared (SWIR) portion of the electromagnetic spectrum (Clark *et al*. 1990). Iron oxides and hydroxides have low reflectance in the visible portion (RGB) and high reflectance in the near infrared (NIR), so the Visible-Near Infrared (VNIR) wavelengths are very useful for recognizing these minerals (Clark 1999; Hunt 1977). For the study of the regional structure and ore formation prognosis, geological lineament extraction has great significance for the manifestation of deep geological structures in the surface of the earth and zones conducive to mineral formation (Han *et al*. 2018; Mohamed *et al*. 2021).

This study integrates diverse data sets including those from Advanced Space-borne Thermal Emission and Reflection Radiometer (ASTER) images, Shuttle Radar Topography Mission (SRTM), geological maps, field surveys and microscopic studies for further gold prospecting in the Nholi area, central Tanzania. Shaded relief maps created from the SRTM Digital Elevation Models (DEMs) using varied azimuth and elevation angles of simulated sun illumination were used for geological lineament extraction (Singh *et al*. 2007; Soulakellis *et al*. 2006). Statistical analyses of lineament trends and density were used to investigate the structure of the study area. Hydrothermal alteration minerals can be discriminated and identified using the short-wavelength infrared (SWIR) sensors of ASTER imagery (Abrams *et al*. 2002). ASTER False Colour Composite (FCC) (bands 321 in RGB), band ratios (BR) (2/1, 7/6) and Relative Absorption Band Depth (RBD) methods were first used for delineating the alteration mineral areas associated with gold mineralization (Alarifi *et al*. 2022; Salem *et al*. 2016; Testa *et al*. 2018). Field survey and microscopic study were used for petrographic investigations and verification of remote sensing results.

The obtained results indicate that the study area shows different structural trends, which reflect multiple episodes of deformation. The employed image processing techniques proved efficient in revealing alteration zones around the known gold deposits and in identifying new prospects. Along the Nholi prospect, the microscopic analysis of sulphide minerals revealed syn- and post-shearing characteristics.

GEOLOGICAL SETTING

The Nholi area lies west of Dodoma, the capital of Tanzania, approximately 50 km from the city centre. The area is located between the latitudes of 6°0'57.60"S and 6°17'20.40"S, and the longitudes of 35°22'15.60"E and 35°39'36"E, respectively, with an approximate surface area of 966 km² (Fig. 1). It lies within the Archean Tanzanian Craton, which is bordered by the Usagaran Belt in the south, the Mo-

zambique Mobile Belt in the east, the Ubendian Belt in the west, the Nyanzian and Kavirondian Supergroups in the north, and by the Karagwe-Ankolean Supergroup in the northwest (Fig. 1). The Craton is divided into three major terranes; the Nyanzian and Kavirondian Supergroups of northern Tanzania around Lake Victoria and basement of older rocks, the Dodoma Complex of Central Tanzania (Geological Survey of Tanzania 2000). The Dodoma Complex is a Meso-Neoarchean geological unit consisting of migmatitic gneisses predominantly of sedimentary origin and granitoids intercalated by narrow greenschist to amphibolite facies (Kamihanda *et al*. 2018). These geological units are considered to be the oldest metasedimentary rocks (3.6 Ga) that were intruded by granitoids (2.8 to 2.6 Ga) and later covered by volcanic rocks (Leger *et al*. 2015; Kaminanda *et al*. 2018). The Dodoma complexes are characterized by the presence of the NE-SW and NNW-SSE trending dyke swarms of the Paleoproterozoic to Mesozoic age (Leger *et al*. 2015).

Locally, the geology of the study area is dominated by the homogeneous Neoarchean sequence of gneisses, major granitoids and less common metavolcanics (Fig. 2). Intrusive rocks are broadly subdivided into older and younger suites. Rocks of the older igneous suite consist of granitic augen gneiss, mafic pyroxene gneiss and various tonalitic orthogneisses (Kamihanda *et al*. 2018), and those of the younger suite of tonalite, granites, gabbro, monzonites, granodiorites, metabasites, syenites and peridotites (Kabete *et al*. 2008). Metasedimentary rock units (Fig. 2) comprise quartz-chlorite-amphibole schists, quartz-mica schists, amphibole schists, corundum schists, hornblende schists and quartzites (Kamihanda *et al*. 2018). Quaternary sediments include clastic and chemical deposits that reflect the on-going erosion associated with tectonic processes and the uplift in the Cenozoic East African Rift System, the eastern arm of the rift, crossing the Dodoma area where the basement outcrop is often extensively covered by residual soils, alluvium and mbuga deposits (Fig. 2).

METHODS AND DATA

SRTM data obtained by using the radar C-band at 3 arcsec (90 m at the equator) were acquired from the United States Geological Survey (USGS) (https://earthexplorer.usgs.gov/). The SRTM data (acquired on September 23, 2014) were used in this study to generate shaded relief maps and the three-dimensional representation of the area's terrain. The shaded relief maps allowed us to highlight linear features related to the geomorphological data, which are not identified in optical images (Ganas *et al*. 2005; Saadi, Watanabe 2008). Using the ER Mapper 7.0 software,

shaded relief images were generated from the SRTM data applying the Analytical hill-shading technique. This technique is used to simulate the topographic illumination under different artificial light directions by introducing both altitude and azimuth parameters. (Abdelouhed *et al.* 2021). Various azimuth and elevation angles of the simulated sun illumination were used in this study to enhance the extraction of geological lineaments (Schowengerdt 2007; Smith, Wise 2007). The extracted lineaments were manually mapped through the on-screen digitization process based on the tone and texture of shaded relief maps and drainage patterns. The extracted lineaments were statistically analysed to create rose diagrams and to display the distribution of trends. The rose diagram was shown as directional trends at 15-degree intervals. Individual lineament lengths were statistically analysed and plotted on frequency distributions of lineaments using the Arc GIS 10.7 software. A kernel density algorithm (Silverman 1986) was used in
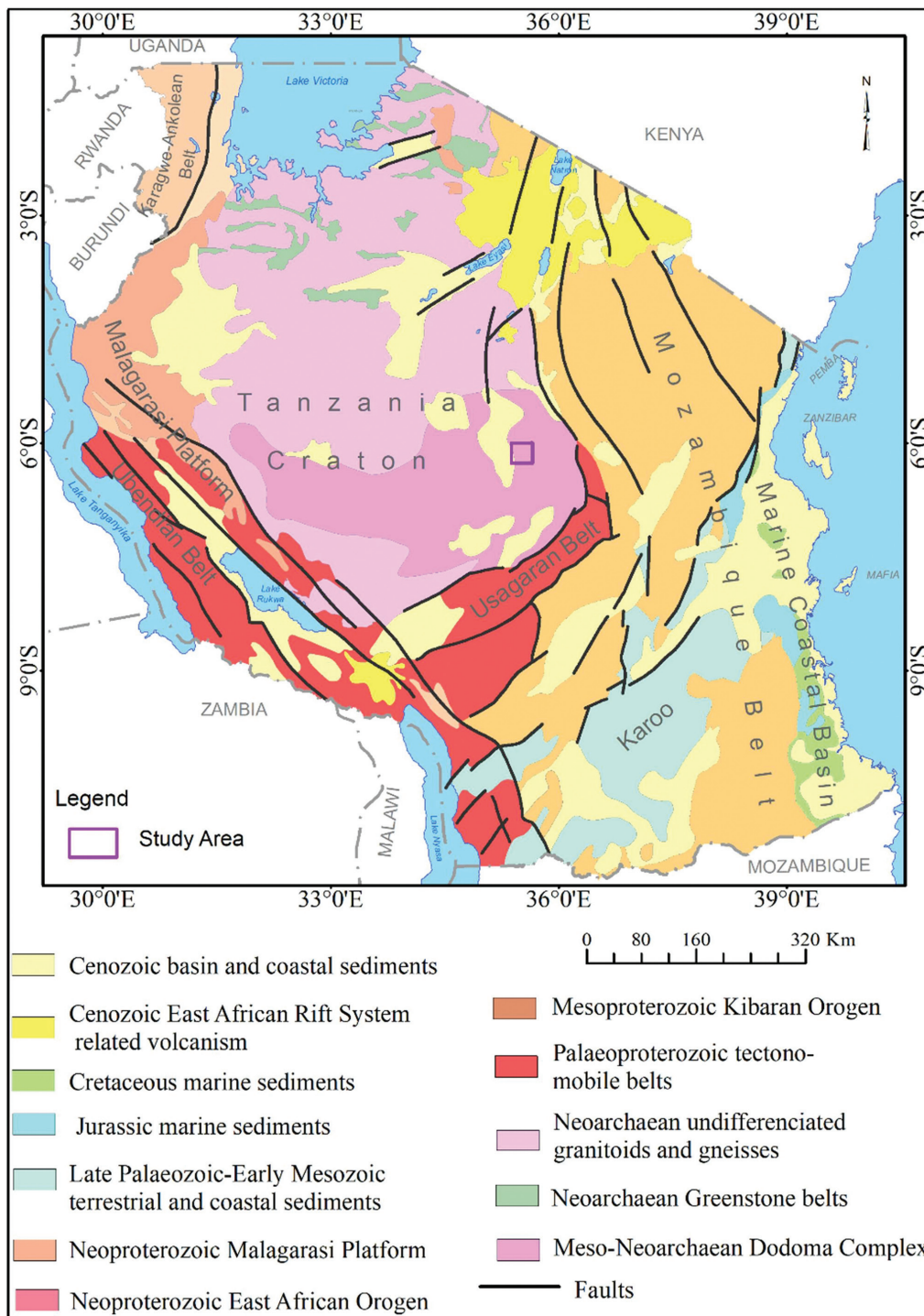

Fig. 1 Geological map of Tanzania showing location of the study area (purple box) and the major rock units together with Archean Granite-Greenstone Belts (Leger *et al.* 2015; Pinna *et al.* 2004)

3

calculations of the lineament's density map with a resolution of 1 km to show the spatial distribution of the geological lineaments in the study area. The total lengths of the lineaments were used for generating the lineament density map. Three zones of lineament density (high, medium and low) were distinguished using gradient colours. The high-density anomalies usually represent a fault or fold development area, whereas low-density anomalies represent a relatively stable tectonic area (Han *et al.* 2018). The data were

processed using the ER Mapper 7.0 software and the processing of thematic data was carried out using the QGIS 3.28.1 software.

One cloud-free ASTER Level 1b image (radiance at sensor) acquired on August 23, 2006 was used for the mapping of the hydrothermal alteration in the study area. The Fast Line-of-sight Atmospheric Analysis of the Spectral Hypercubes (FLAASH), an atmospheric correction module of the ENVI 5.1 software, was used as an essential component for the con-
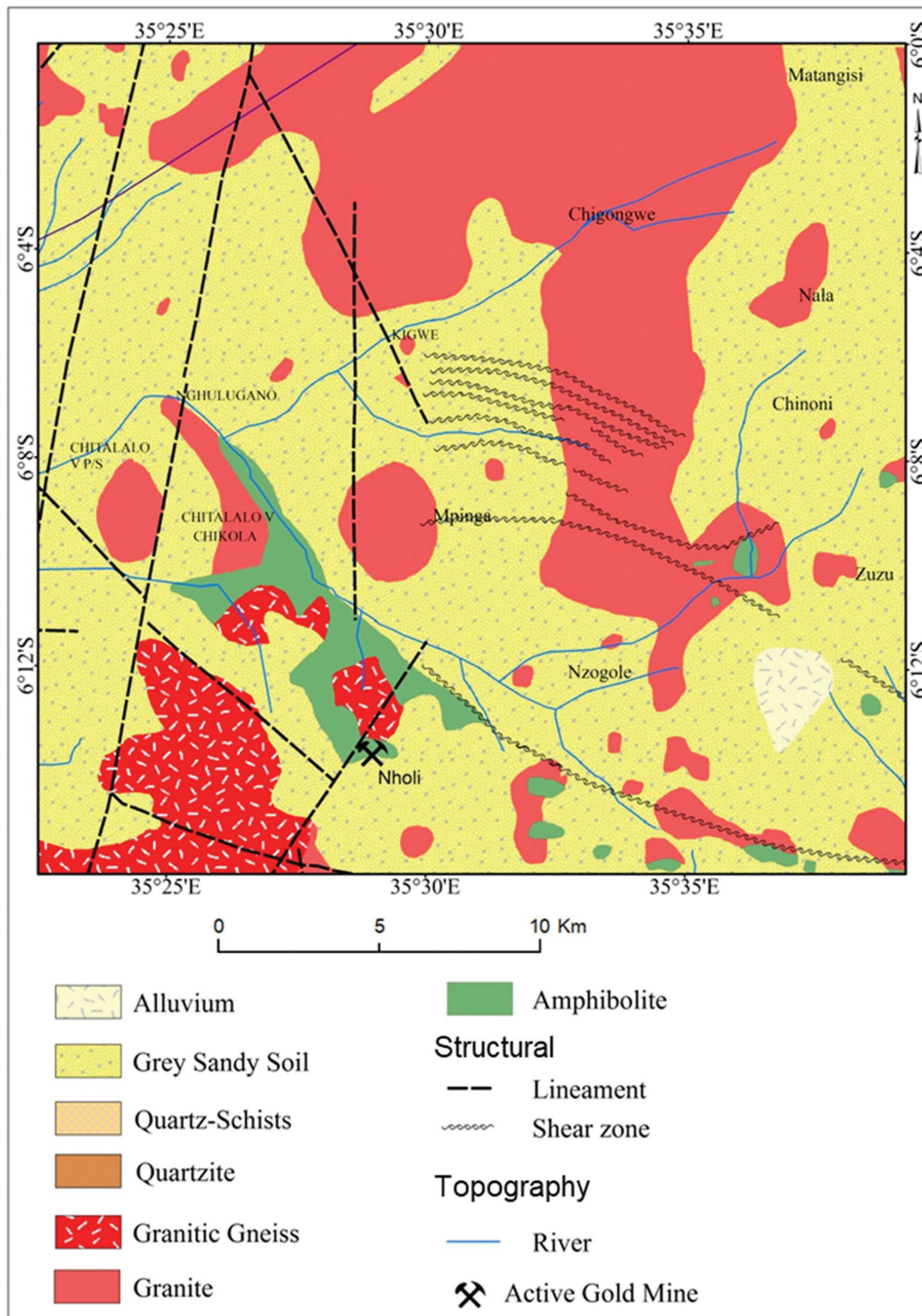

Fig. 2 Geological map of the Nholi area (modified after Geological Survey of Tanzania 2000)

4

version of the radiance measured by the sensors into surface reflectivity (Matthew *et al*. 2000). Previous studies have demonstrated that specific hydrothermally altered minerals such as chlorite, quartz and muscovite can be identified based on the spatial and spectral resolution of remote sensors (Pour, Hashim 2011; Rowan *et al*. 2006). Seven spectral bands were used in this study, including three VNIR bands and four SWIR bands. VNIR: band 1 (0.52–0.60 μm), band 2 (0.63–0.69 μm), band 3N (0.78–0.86 μm) with 15 m spatial resolution; SWIR: band 4 (1.600–1.700 μm), band 5 (2.145–2.185 μm), band 6 (2.185–2.225 μm), band 7 (2.235–2.285 μm) with 30 m spatial resolution (Abrams 2000).

Identification and delineation of iron ore mineral deposits can be accomplished using ASTER band ratios. ASTER band ratio 2/1 was calculated to highlight pixels with intense ferric iron absorption, which articulates the reflectance reduction in band 1 in relation to band 2, allied with ferric-iron absorption due to hematite or goethite-rich units (Abay *et al*. 2022; Alimohammadi *et al*. 2015; Gopinathan *et al*. 2020). ASTER RGB 321 was applied to highlight the areas of vegetation and mineral alteration (Brandmeier *et al*. 2013). ASTER band ratio 7/6 was used to detect muscovite, which is a useful tool in mapping the effects of hydrothermal alteration processes. In addition, the Relative Absorption Band Depth (RBD) was used to detect alterations in intensities of clay minerals in the study area. RBD is a proven technique for identifying distinctive absorption properties, in which the numerator is the sum of the bands representing shoulders and the denominator is the band located nearest the absorption feature minimum (Crowley *et al*. 1989; Masoumi *et al*. 2021). One type of RBD, i.e. RBD5, which was assigned a single band pseudo colour to enhance the clay mineral alteration zone, was tested in this study. The RBD ratio was derived based on Crowley *et al*. (1989) as RBD5 = [(band 4 + band 6)/ (band 5)].

Field Survey and XRD analysis

The field survey focused on the Nholi Prospect, which is known for its gold mine, shear zone and alteration zones. The study done by Kamihanda *et al*. (2018) in the Nholi Prospect by surface geological mapping and the ground magnetic survey revealed a NW-SE trending shear zone with predominantly phyllic and iron oxide alterations observed in the field. However, the previous investigation focused only on the Nholi Prospect without the extension of the shear zone that controls mineralization, petrography and XRD analysis to ascertain the existence of hydrothermal alteration minerals. Therefore, in this study various methods were used for the identification of new prospects of high-potential alteration zones associated with gold mineralization.

The field survey was carried out in the Nholi area for collecting rock samples and ground truth verification of remote sensing data using GPS (average accuracy of 3 m). Rock samples for laboratory analysis were collected in the areas of the identified hydrothermal alteration zones. Petrographic studies of the representative rock samples, quartz veins and ore samples collected from the Nholi mine were carried out using a Nikon ESCLIPSE LV100N POL polarizing Microscope equipped with a charged-166 coupled device Camera. XRD analysis was performed using a Rigaku FKOD10-015 X-ray Diffractometer equipped with 0.5 mm of lead (Pb) equivalent at the Department of Earth Resources Engineering, Kyushu University, Japan.

RESULTS AND DISCUSSION

Remote sensing

Shaded relief maps detected a total of 248 lineaments, mostly running in the NE–SW direction. Subordinate trends are mainly WNW-ESE, features, which are trending NW–SE, N–S and E–W, were also mapped (Fig. 3). In the shaded relief maps, the incoming illumination (NW and NNW) that is perpendicular to the prevailing trend of lineaments (NE–SW) revealed most of the geological lineaments in the study area. A low sun-elevation angle (35º to 45º) proved more effective for lineament detection in all directions. As the solar azimuth angle editor in ER Mapper allows manually operating and changing the light-source directions and sun elevation to avoid directional bias, we were able to investigate all the possible sun azimuth directions and elevations with minor angles for more accurate results. The lineaments extracted from the all-sun azimuth directions and elevations were integrated into a single image. The density map (Fig. 3) indicates that areas of high lineament densities looking like longitudinal shapes are located in the eastern and southern parts of the study area. Compared to the rest of the regions, the density of lineaments in the central part of the study area is low.

ASTER FCC (RGB 321) typically shows mineral alteration areas in green tones with vegetation in red tones. The study area is sparsely vegetated along river channels and valleys (Fig. 4a). Halite and carbonates show bright reflectance in the middle of the study area along the valleys and low-lying areas of the semi-arid region. ASTER band ratio 2/1 displays a strong ferric iron absorption feature (shown in red colour) due to secondary processes, typically goethite and hematite alterations. These oxide phases are mainly distributed along the shear zones with recognizable three distinct prominent alterations subparallel to each other trending in the NW-SE direction (Fig. 4b). In Fig. 4c
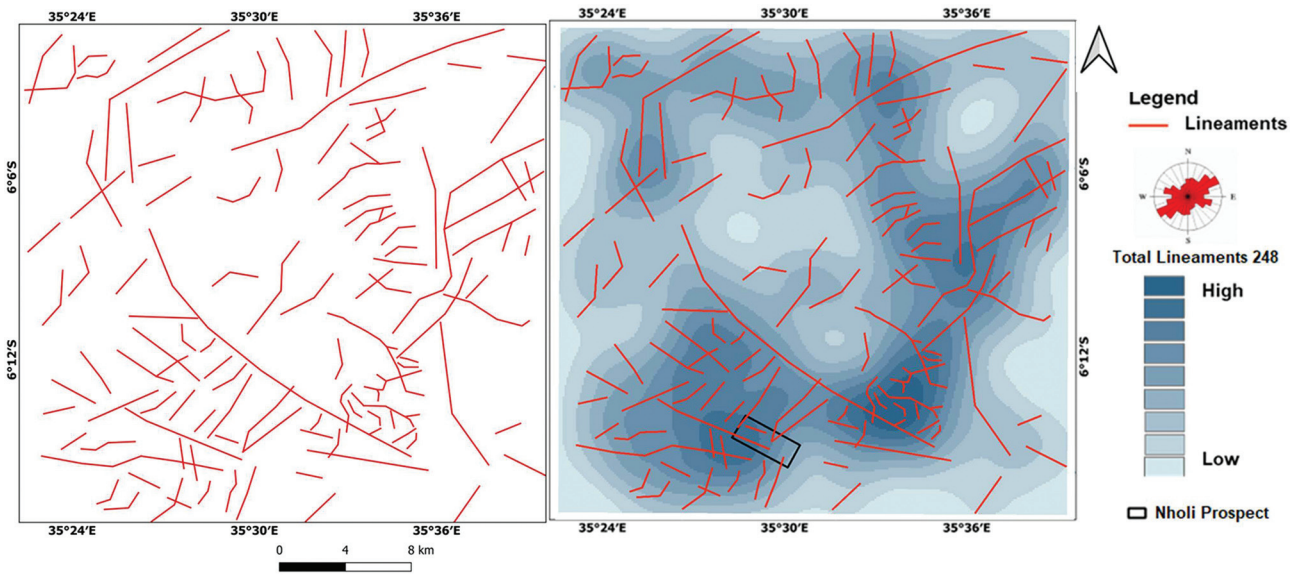
Fig. 3 Lineaments extracted from SRTM DEM with a rose diagram and high structural complexities, fractures/faults density overlain by the mine location in the Nholi prospect
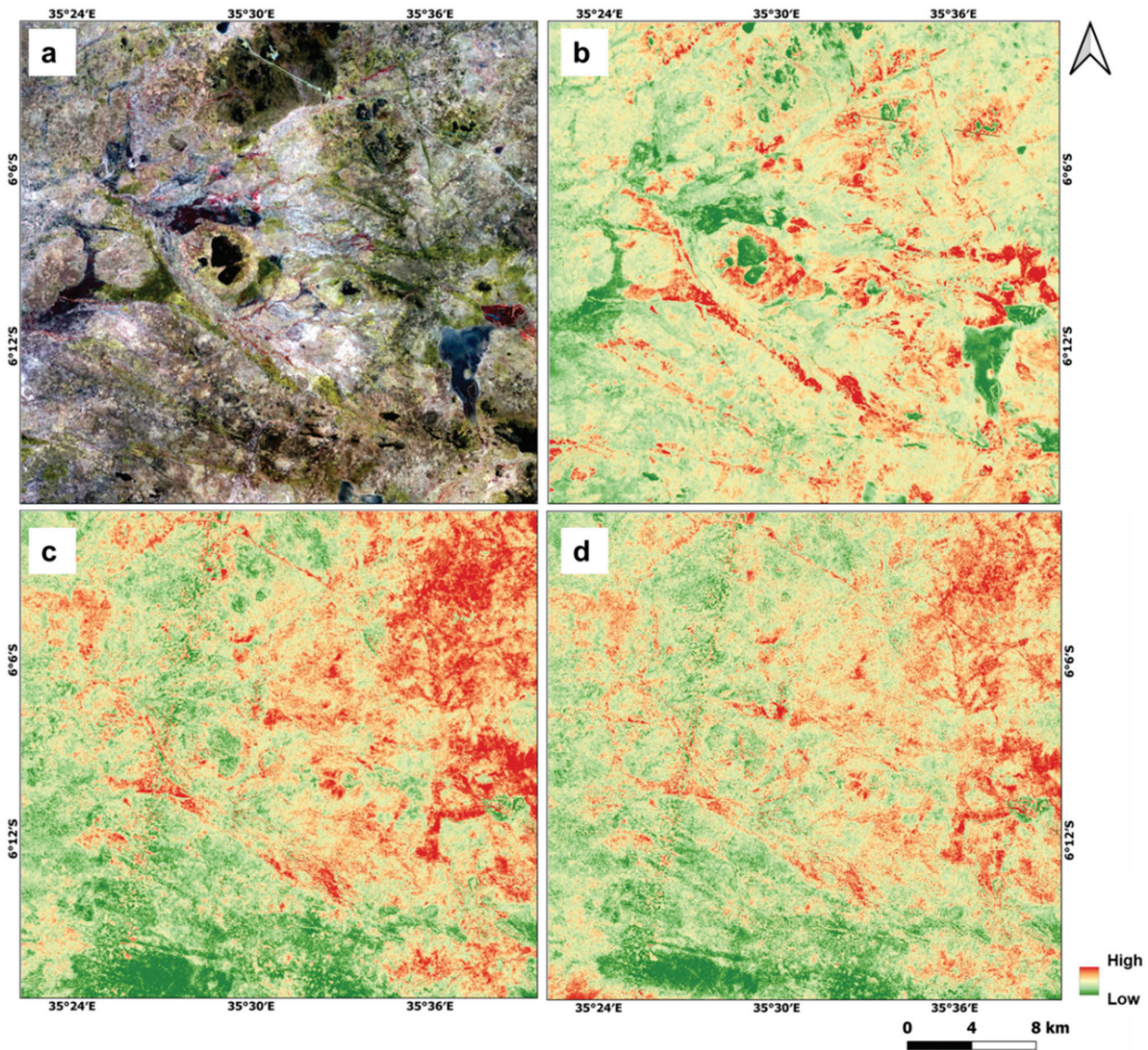

Fig. 4 Results of ASTER Alteration mapping in the Nholi Prospect: a) RGB 321 map to highlight vegetation (in red) and mineral alteration areas (in green), b) band ratio image of 2/1 to highlight the distribution of iron oxides, c) band ratio 7/6 to show the distribution of muscovite bearing minerals, and d) RBD 5 image map to delineate phyllic alteration

6

(band ratio 7/6), the hydrothermally altered zones appear as red colour on the eastern to northern parts and along the NW–SE trending shear zone. This can be due to the fact that muscovite spectrum has low reflectance in band 6 and relatively high reflectance in band 7 as suggested by Hewson *et al*. (2005). RBD5 was applied to delineate the phyllic alteration mineral assemblages such as white micas, illite and smectite with spectral characteristics that show a strong Al-OH absorption feature, which is classically positioned at 2.2 µm. In this study, mineral alteration assemblages are shown in red on the eastern margin of the study area. Along the shear zone from SE to NW, it is possible to identify a prominent mineral alteration assemblage, which further, from the centre (at branch off point) towards the northern part of the study area, forms a semi-circular shape (Fig. 4d).

Field survey and XRD analysis

Figure 5 shows the interpreted structural geology map, the ASTER image and the field survey conducted in the Nholi Prospect. The identified remote sensing signals (lineaments and alteration maps) are evident on the ground with their respective sample locations. The identified signals are trending in the NW–SE direction so that the alteration zones are controlled by the shear zone along the Prospect.
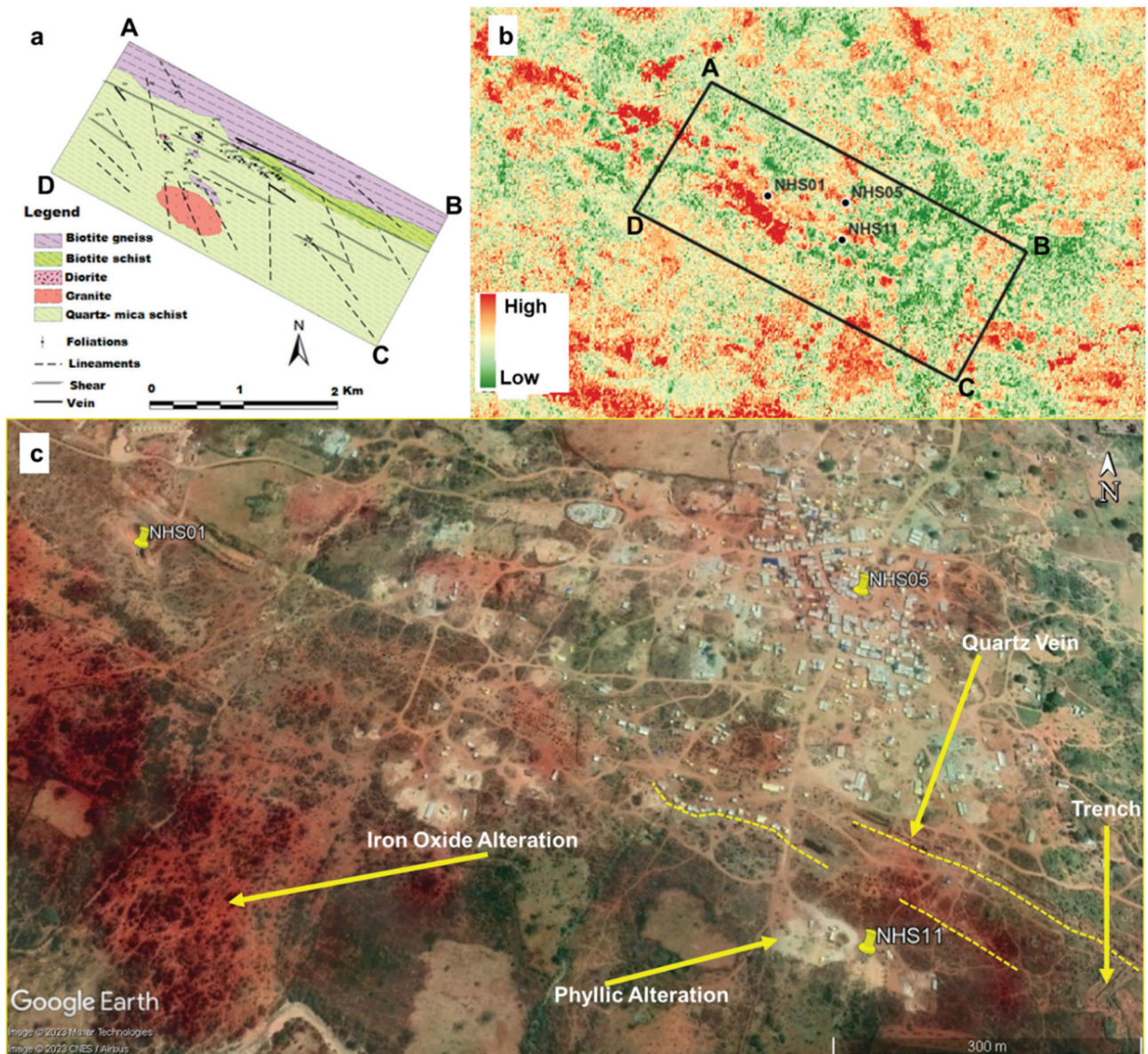

Fig. 5 The link between Structural Geology and the Identified Remote Sensing Signals: **a)** the geological map of the Nholi Prospect (Kamihanda *et al*. 2018), **b)** the alteration map of ASTER image calculated from b2/b1 showing the location of the representative samples used in this study, and **c)** the satellite image from Google Earth overlain by the alteration map of the Nholi Prospect showing actual sample locations, quartz veins with their respective alteration zones. A, B, C and D represent corner coordinates of the UTM Zone 36S (774325, 9310112), (777722, 9308268), (776955, 9306878) and (773479, 9308734), respectively
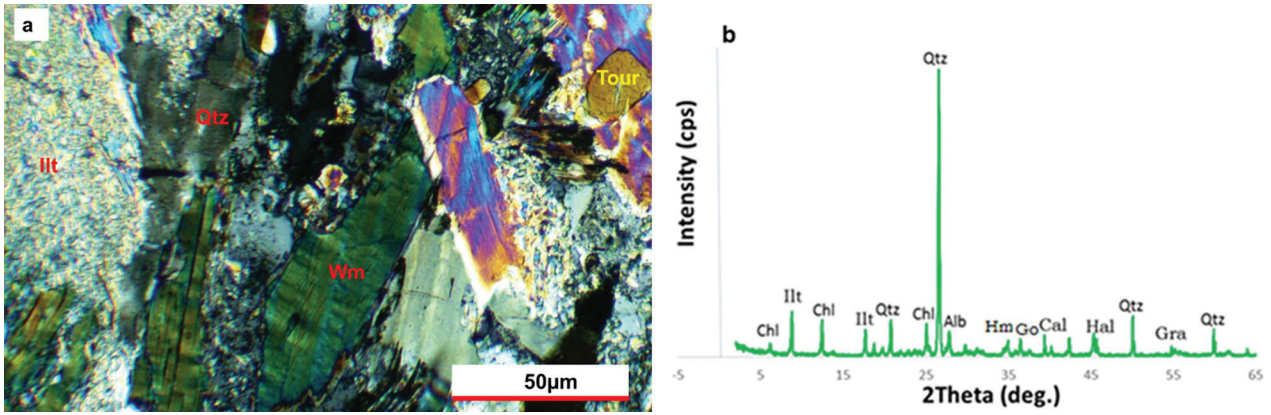
Fig. 6 Mode of occurrence of hydrothermal minerals and XRD from the Mica Schist sample **NHS 11** of the Nholi Prospect: **a)** thin section photomicrograph observed through a crossed polarized light microscope showing alteration mineral assemblages, **b)** bulk sample mineralogy showing XRD peaks. Abbreviations: Ilt – Illite, Qtz – Quartz; Wm – White Mica, Tour – Tourmaline, Chl – chlorite, Alb – albite; Cal – calcite; Hal – Halite; Goe – goethite, Gra – graphite, Hm – hematite
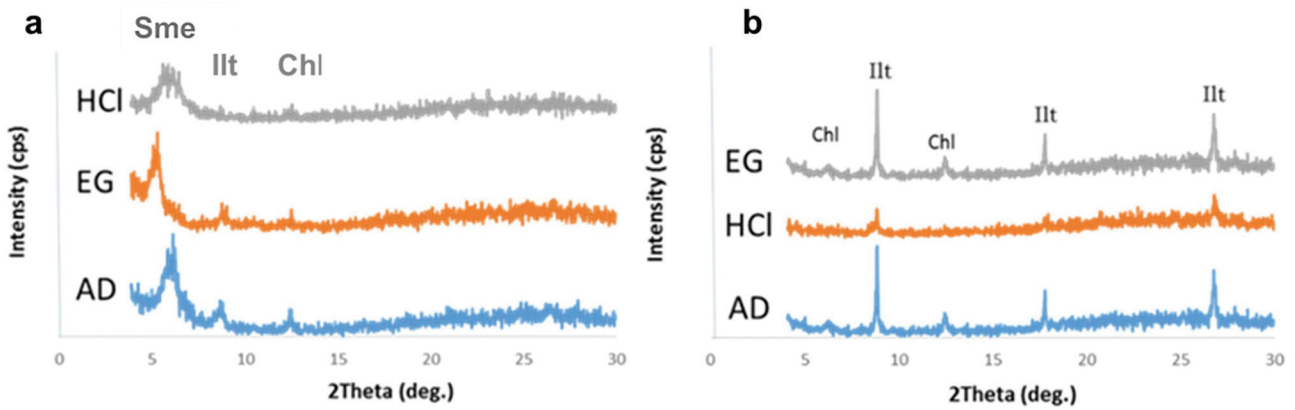

Fig. 7 XRD patterns for oriented samples for clay mineral analysis in the Nholi Prospect: **a)** Smectite, Illite and Chlorite peaks from the sample **NHS01**, and **b)** Illite and Chlorite peaks from the sample **NHS 11**. Abbreviations: AD – air dried samples, HCl – hydrochloric acid treated samples, and EG – ethylene glycol treated samples
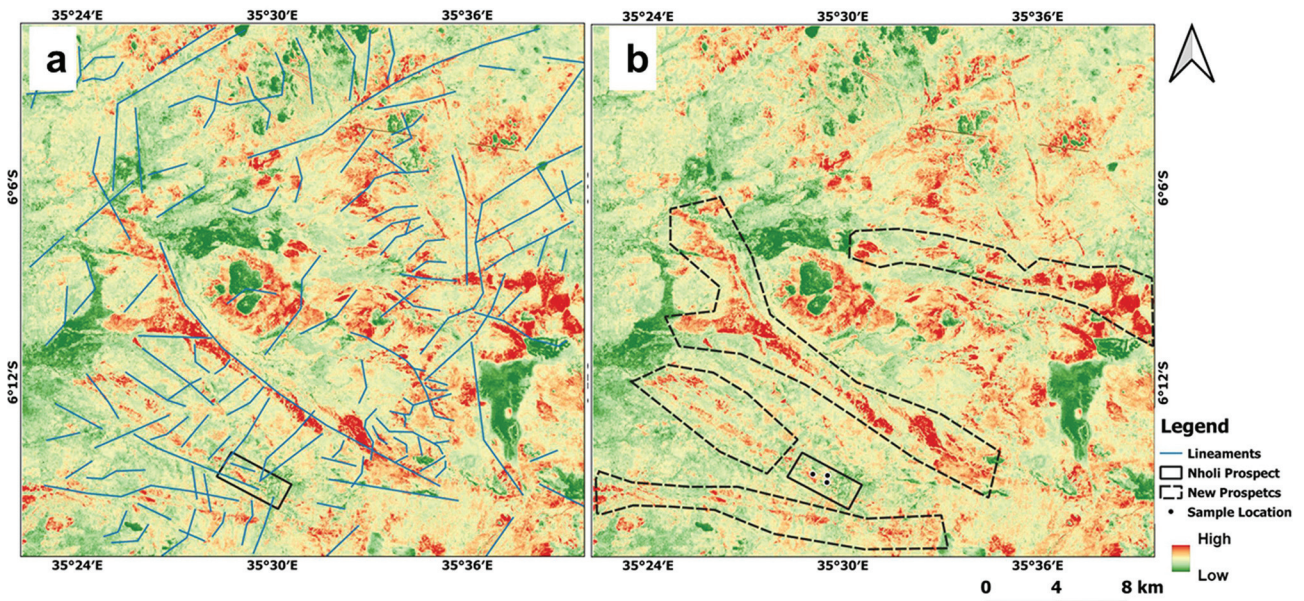

Fig. 8 Relationship between the results of band ratio indices and extracted lineaments: **a)** positive correlation between extracted lineament and ASTER band ratio 2/1, and **b)** the identified new prospects based on the results of ASTER, SRTM and the known mine location (Nholi Prospect)

Thin section photomicrographs of the altered mica schists showing the existence of hydrothermal minerals provide the evidence of the secondary mineralization of white micas and illite as they appear to replace the primary crystals with tourmaline as an accessory mineral that overprints the white micas (Fig. 6a). In addition, the bulk mineralogy of the sample detected different alteration minerals including goethite and hematite in iron oxide alteration zone (Fig. 6b). Mineralogy of the fine-grained samples by XRD detected illite, smectite and chlorite in the phyllic alteration zone (Fig. 7).

It is clearly seen that the results of the field survey, petrography and XRD coincide with those of remote sensing signals. The remote sensing signal results together with those of the field work and the interpreted geological map indicate a close relationship between the extracted lineaments and hydrothermal alteration zones.

The lineaments distribution map overlaid on the alteration map and Nholi mine was found to be concentrated on the high structural complexities, fractures/faults density. Also, there was a positive correlation found to exist between the extracted lineaments and hydrothermal alteration zones (Fig. 8a). Moreover, the identification of the alteration zone around the known gold Prospect allowed extending the location of new potential areas in the vicinity (Fig. 8b).

Structural analysis and interpretations

As proved by structural analysis, field observations and interpretation of satellite images, gold and sulphide-bearing quartz lodes in the Nholi Prospect occur in the metasedimentary rock within the shear zones (Fig. 9), and they are not recorded outside of it. These quartzes lodes are concordant to the main structural fabrics of the metasedimentary host-rocks.

The ductile and brittle structural elements recorded and analysed in the metasedimentary host-rocks include foliation, lineation, folding, faulting, and shear-related structures. As shown by trend analysis, these rocks have two foliation attitudes (S1 and S2), corresponding to different deformation events in the study area (Fig. 9a). However, the S1 fabrics related to the earlier deformation event in the Nholi area are rare. S1-foliation striking E70-85W and moderately to slightly dipping (25°–30°) towards SE, is associated with the E-W-thrust faults in the study area (Fig. 9a). These foliation planes are parallel to the axial plane of the E-W-trending F1 minor folds with a fold axis plunging 15° towards the east (Fig. 9b). Near the thrust belt, the S1-foliation is cut by a sub-vertical shear foliation (S2) (Figs 9a, 9b). The S2-foliation is striking N30-40W and is steeply dipping (75°–85°) towards NE and SW. The F2 folds in the metasediments exist as open to tight, and upright with syncline

and anticline forms (Figs. 9b, 9c). On the stereo net, S2-poles show the sub-vertical to steeply NE- and SW-dipping planes, gently plunging in the NW-direction (Fig. 9b). Well-developed NW–SE lineations (L2) are commonly horizontal in the sub-vertical S2-foliation planes (Fig. 9d). These lineations are parallel to the F2 fold axes, however, within the shear zone, this lineation occurs at an acute angle (~10°) to the measured F2 fold axes, which indicates that the F2 fold-event coincides with the dominant dextral oblique shearing (Fig. 9b).

According to the brittle deformation analysis results, the oldest deformation fabrics in the metasedimentary rocks are E-W-thrust faults, and the associated S1-foliation. These fabrics have developed under the N–S compressional regime (shortening). The metasedimentary rocks represent the footwall of the E-W-thrust in the study area (Fig. 9a). This regime is overprinted by a dominant dextral oblique-slip regime along the NW–trending shear zone (Figs 9a, 9e). Based on the fault-slip data, this regime is characterized by a paleo stress field that has an E–W trending $\sigma1$ (steeply plunging), N–trending $\sigma3$, and $\sigma2$ nearly perpendicular to the earth surface (Fig. 9e). The regime-controlled conjugate set of oblique-slip faults includes NW right-lateral and NNE–SSW trending left-lateral faults (Fig. 9e). Post-orogenic extensional regime has been recorded in the metasedimentary host-rocks that are characterized by NNW–SSE, and E–W normal faults (Figs 9c, 9f, 9g).

Kinematic indicators are observed on different scales ranging from the outcrop-scale to the microscopic one both in quartz lodes and in metasedimentary host-rocks. In some places, quartz lodes occur in the form of asymmetric sigmoidal aggregates within the main NW-dextral shear zone (Fig. 9f). Furthermore, well-developed σ-porphyroclasts of hornblende and sulphide in the metasedimentary host-rocks and sulphide in quartz lodes indicate that they have rotated dextrally during the main shearing event (Figs 9h, 9i).

The structural analysis of the mineralized site and its surroundings indicates that these rocks have experienced three deformation events (D1, D2 and D3). Traces of the D1-event in the Nholi area are poorly preserved. However, some traces of its fabrics could be observed, especially, along the E–W thrust and the E–W fold (DF1). The N–S upright folds (DF2) and the conjugate NW- dextral and NNE- sinistral shear sets represent the surviving signs of the D2-event, while E–W and NW–SE normal faults are the extant traces of the D3-event, which is an extensional stage expressed by E-W and NW–SE normal faults. The D1 and D2 events are most likely related to the late-stage collisional shortening of the Pan-African Mozambique orogeny (e.g., Kwelwa 2017); however, D3 is most probably related to the East African Rift System.
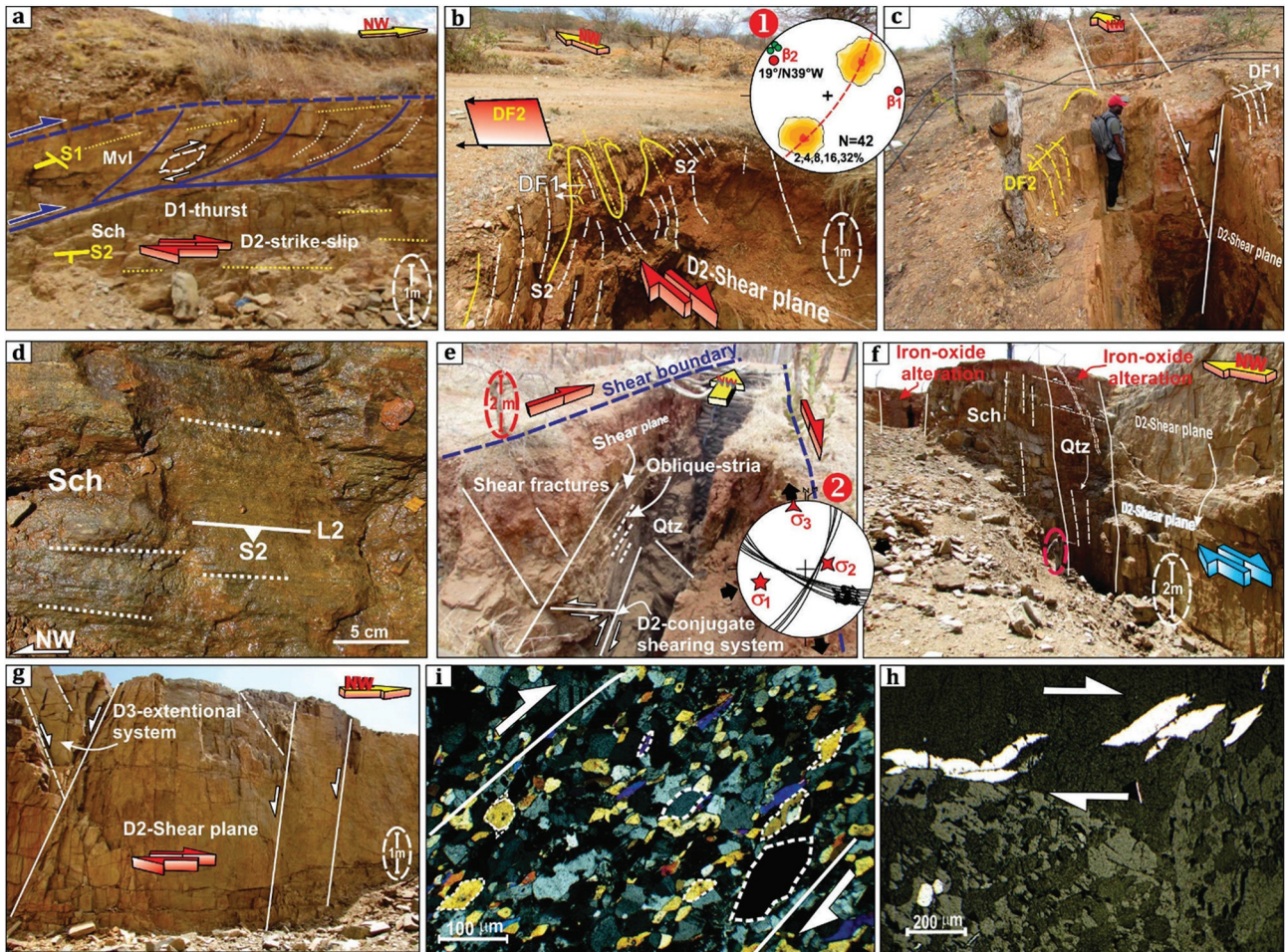
Fig. 9 Structural features and the related analysis of quartz lodes and metasedimentary host-rocks in the Nholi area: **a)** D1-thrust contact between schist and metavolcanics cut by the D2-strike slip fault, **b)** interference between E-W-F1 (β1) and NW-F2 folds (β2), the S2 foliation, with shearing development (poles to S2-foliation show fold axis (β2) gently plunging NW, whilst F1-fold axis (β1) is sub-horizontal to gently plunging E), **c)** the relationship between D1, D2, and D3 structures (DF1 is superimposed by DF2 and D2-stick slip shearing, however, these structures are transected by D3-normal faults), **d)** horizontal stretching L2-lineations in vertical S2-foliation in metasedimentary host-rocks, **e)** NW- dextral shearing anatomy hosting gold bearing quartz lode with paleostress kinematic configurations indicate an E–W- and N–S-trending σ1 and σ3, respectively, **f)** hydrothermal alteration associated with gold and sulfide-bearing quartz and controlled by NW- dextral shearing, and **g)** the relationship between D2, and D3 structures. Photomicrographs (in XPL view – parallel to L2-lineations) of microstructural shear-kinematic indicators in the metasedimentary host-rocks and quartz lodes respectively: **i)** asymmetric σ-porphyroclasts of hornblende and pyrites indicate a dextral sense of shearing, and **h)** σ-porphyroclasts of pyrites in quartz lode indicate a dextral sense of shearing and reflect syn-kinematic properties, however, later, subcircular-shaped pyrites (near the scale bar) indicate the post-tectonic mode of formation. **Stereographic projections** (numbers in red circles): 1 – equal-area stereographic projections (lower hemispheres) showing poles to foliation, and fold axes (β) showing mineral lineation related to F2-folds and F1-fold axes measured in the field (in green dots), 2 – lower-hemisphere equal-area projection of fault planes, slickensides, and constructed paleo-stress configurations (red stars are σ1, σ2 and σ3). **Abbreviations**: S1 – E-W-trending foliation, S2 – NW-SE-trending foliation, L2 – D2-lineations, Mvl – metavolcanics, Sch – metasediments, Qtz – quartz lodes

Structural control of mineralization and hydrothermal system

According to Kamihanda *et al.* (2018), gold mineralization in the Nholi Prospect takes place in vein systems that are structurally controlled, sub-vertical dipping, hosted in quartz-mica schist or biotite gneiss units, which are associated with copper and arsenic based on soil and whole rock geochemistry.

In a broader sense, orogenic gold and sulphide de-posits were formed during late stages of the deformational-metamorphic–magmatic history of the evolving orogeny, syn-kinematic with the main penetrative deformation stage of host rocks (Goldfarb *et al.* 2001; Groves *et al.* 2003; Ibrahim *et al.* 2014, 2016). The Nholi area has internal evidence of poly-phase (three deformational events) indicated by brittle-ductile shearing deformation. The main deformation event in the Nholi area is (D2) characterized by stress regime, with σ1 trending E–W and σ3 trending N–S, control-

led NW dextral and NNE-sinistral strike slip faulting under brittle-ductile conditions.

Structural controls of the gold and sulphide-bearing quartz lodes in the Nholi Prospect were observed on various scales, ranging from map- to outcrop- and microscopic scales (Fig. 9). Quartz lodes were emplaced within the N- to NW-trending shear zone and were strike-parallel to those of the host-rock D2-tectonic fabrics e.g., F2-axial plane, S2- foliation, L2-lineation, and NW-dextral shearing (Fig. 9). This suggests that their emplacement was controlled by D2-tectonics, which seems to act as a basic control of quartz distributions in the Nholi Prospect.

The occurrence of asymmetric sigmoid-shaped quartz lodes within the sub-vertical NW-shearing foliation indicates a dextral shear sense (Fig. 9f). Furthermore, the quartz lodes show no evidence of cross-cut field relationships to D3-structures, but rather the evidence of being transected by D3-tectonic structures (Figs 9c, 9g). Sulphide minerals (pyrite) in both quartz lodes and schist host-rocks show syn-shearing characteristics: they are deformed and serrated from top to right, parallel to the host shear zone boundaries and its shearing foliation, and further reflect a dextral sense of shear (Figs 9h, 9i).

In many Archaean greenstone belts, regional gold bearing structures are localized within tectonic domains with suitable geological settings involving terrain boundaries that act as control crustal-scale plumbing systems of mantle-derived magma and hydrothermal fluids (Goldfarb *et al*. 2005; Phillips, Powell 2010; Kwelwa 2017). Probably, these hydrothermal fluids were variably sourced and were concentrated along kilometre-scale brittle-ductile shear zones (Dunn *et al*. 2021).

In the Nholi area, the spatial/temporal relationship between regional structures (D2), gold mineralization, and syn-tectonic granitoids likely links (but does not confirm) the hydrothermal system to the mantle-derived magma solution (e.g., Goldfarb *et al*. 2005; Phillips, Powell 2010; Kwelwa 2017). This is likely to have occurred during D2-shearing and the emplacement of syn-tectonic granitoids in the study area. This hypothesis can be supported by: 1) the D2-structural control of gold-sulphide-bearing quartz lodes and related hydrothermal alterations (Figs 9h, 9i); 2) the emplacement of granitoids in the Nholi area, which is controlled by D2-shearing brittle-ductile conditions (Figs 2, 5a). Additionally, further north of the study area, some of the granitoids rocks were emplaced syn-tectonically along NW-structural fabrics (D2) (e.g., Kwelwa 2017).

CONCLUSION

The analysis of ASTER imagery using integrated image transformation methods (including; RBD, BR, FCC, and filtering) in combination with structural data analysis using SRTM DEM data and field investigations performed within the framework of this study allowed us to deepen the understanding of the distribution, litho-structural setting, and hydrothermal alteration related to gold and sulphide-bearing quartz lodes in the Nholi area. The techniques applied in the study area proved efficient in revealing alteration zones around the known gold deposits and in identifying new prospects.

The microscopic study of sulphide minerals (pyrite) exhibited syn- and post-shearing characteristics along the Nholi prospect. They are deformed and serrated from top-to-right, parallel to the host shear zone boundaries and its shearing foliation. The spatial relationship between regional structures (D2), gold-sulphide mineralization, and syn-tectonic granitoids is likely to link the hydrothermal system to the mantle-derived magma solution due to D2-tectonic event as a model of hydrothermal and syn-kinematic ore formation under brittle–ductile conditions. Thus, the mineralization in the Nholi area is mostly controlled by D2 deformation event. This event is characterized by a stress regime with σ1 trending E–W and σ3 trending N, that mainly activated the conjugate NW right-lateral and NNE–SSW trending left-lateral strike-slip faults, likely during the granitoids emplacement.

The results obtained from this study proved the existence of a relationship between a highly tectonized terrain and gold-sulphide mineralization. In this way, the priority in the gold exploration target in the Tanzania Craton should be given to the adjacent high-grade tectonic-metamorphic setting, such as metasedimentary belts governed by extensive brittle-ductile conditions.

REFERENCES

Abay, H.H., Legesse, D., Suryabhagavan, K.V., Atnafu, B. 2022. Mapping of ferric (Fe3+) and ferrous (Fe2+) iron oxides distribution using ASTER and Landsat 8 OLI data, in Negash Lateritic iron deposit, Northern Ethiopia. *Geology, Ecology, and Landscapes*. Published online: 11 Oct 2022. https://doi.org/10.1080/24749508.2022.2130556

Abdelouhed, F., Algouti, A., Algouti, A., Ifkirne, M. 2021. Lineament Mapping in the Ikniouen Area (Eastern Anti-Atlas, Morocco) Using Land-

sat-8 Oli and SRTM Data. *Remote Sensing Applications: Society and Environment 23*, 100606. https://doi.org/10.1016/j.rsase.2021.100606

Abrams, M. 2000. The advanced spaceborne thermal Emission and Reflection Radiometer (ASTER) data products for the high spatial resolution imager on NASA's Terra platform. *International Journal of Remote Sensing* 21 (5), 847–859. https://doi.org/10.1080/014311600210326

Abrams, M., Hook, S., Ramachandran, B. 2002. ASTER User Handbook-Advanced Spaceborne Thermal Emission and Reflection Radiometer. *Jet Propulsion Laboratory with California Institute of Technology and NASA.* http://www.pancroma.com/downloads/aster_user_guide_v2.pdf

Alarifi, S.S., Abdelkareem, M., Abdalla, F., Abdelsadek, I.S, Gahlan, H., Al-Saleh, A.M., Alotaibi, M. 2022. Fusion of Multispectral Remote-Sensing Data through GIS-Based Overlay Method for Revealing Potential Areas of Hydrothermal Mineral Resources. *Minerals 12* (*12*), 1577. https://doi.org/10.3390/min12121577

Alimohammadi, M., Alirezaei, S., Kontak, D.J. 2015. Application of ASTER data for exploration of porphyry copper deposits: A case study of Daraloo-Sarmeshk area, southern part of the Kerman copper belt, Iran. *Ore Geology Reviews 70*, 290–304. https://doi.org/10.1016/j.oregeorev.2015.04.010

Brandmeier, M., Erasmi, S., Hansen, C., Höweling, A., Nitzsche, K., Ohlendorf, T., Mamani, M., Wörner, G. 2013. Mapping patterns of mineral alteration in volcanic terrains using ASTER data and field spectrometry in Southern Peru. *Journal of South American Earth Sciences 48*, 296–314. https://doi.org/10.1016/j.jsames.2013.09.011

Clark, R.N. 1999. Spectroscopy of rocks and minerals and principles of spectroscopy. In: *Manual of Remote Sensing*, edited by A.N. Rencz, 3–58. New York: John Wiley.

Clark, R.N., King, T.V., Klejwa, M., Swayze, G.A., Vergo, N. 1990. High spectral resolution reflectance spectroscopy of minerals. *Journal of Geophysical Research: Solid Earth 95 (B8)*, 12653–12680. https://doi.org/10.1029/JB095iB08p12653

Condie, K.C. 1994. *Greenstones through time*. In: Condie, K.C., ed., Archean.

Crowley, J.K., Brickey, D.W., Rowan, L.C. 1989. Airborne imaging spectrometer data of the Ruby Mountains, Montana: mineral discrimination using relative absorption band-depth images. *Remote Sensing of Environment 29 (2)*, 121–134. https://doi.org/10.1016/0034-4257(89)90021-7

Crustal Evolution: Amsterdam, Elsevier, 85–120 pp.

Dunn, S.C., von der Heyden, B.P., Steele-MacInnis, M., Kramers, J.D., Pierre, B.S., Erasmus, R., Harris, C. 2021. Neoproterozoic copper-gold mineralization in the Amani area, southwestern Tanzania. *Ore Geology Reviews 132*, 104070.

https://doi.org/10.1016/j.oregeorev.2021.104070

Gabr, S., Ghulam, A., Kusky, T. 2010. Detecting areas of high-potential gold mineralization using ASTER data. *Ore Geology Reviews 38 (1–2)* 59–69. https://doi.org/10.1016/j.oregeorev.2010.05.007

Ganas, A., Palvides, S., Karastathis, V. 2005. DEM-based morphometry of range-front escarpments in Attica, central Greece, and its relation to fault slip rates. *Geomorphology 65 (3–4)*, 301–319. https://doi.org/10.1016/j.geomorph.2004.09.006

Geological Survey of Tanzania. 2000. Explanatory Notes of Degree Sheet 52_Dodoma. Available at http:www.gst.go.tz

Goldfarb, R.J., Groves, D.I., Gardoll, S. 2001. Orogenic gold and geologic time: a global synthesis. *Ore geology reviews 18 (1–2)*, 1–75. https://doi.org/10.1016/S0169-1368(01)00016-6

Goldfarb, R.J., Baker, T., Dubé, B., Groves, D.I., Hart, C.J., Gosselin, P. 2005. Distribution, Character, and Genesis of Gold Deposits in Metamorphic Terranes. *One Hundredth Anniversary Volume, Society of Economic Geologists.* https://doi.org/10.5382/AV100.14

Gopinathan, P., Parthiban, S., Magendran, T., Al-Quraishi, A.M.F., Singh, A.K., Singh, P.K. 2020. Mapping of ferric (Fe3+) and ferrous (Fe2+) iron oxides distribution using band ratio techniques with ASTER data and geochemistry of Kanjamalai and Godumalai. Tamil Nadu, South India. *Remote Sensing Applications: Society and Environment 18*, 100306. https://doi.org/10.1016/j.rsase.2020.100306

Groves, D.I., Goldfarb, R.J., Robert F., Hart, C.J. 2003. Gold Deposits in Metamorphic Belts: Overview of Current Understanding, Outstanding Problems, Future Research, and Exploration Significance. *Economic Geology 98 (1)*, 1–29. https://doi.org/10.2113/gsecongeo.98.1.1

Han, L., Liu, Z., Ning, Y., Zhao, Z. 2018. Extraction and analysis of geological lineaments combining a DEM and remote sensing images from the northern Baoji loess area. *Advances in Space Research 62 (9)*, 2480–2493. https://doi.org/10.1016/j.asr.2018.07.030

Hewson, R.D., Cudahy, T., Mizuhiko, S., Ueda, K., Mauger, A.J. 2005. Seamless geological map generation using ASTER in the Broken Hill-Curnamona province of Australia. *Remote Sensing of Environment 99 (1–2)*, 159–172. https://doi.org/10.1016/j.rse.2005.04.025

Hunt, G.R. 1977. Spectral signatures of particulate minerals in the visible and near infrared. *Geophysics 42 (3)*, 501–513. https://doi.org/10.1190/1.1440721

Ibrahim, W.S., Watanabe, K., Ibrahim, M., Yonezu, K. 2014. Controls on quartzite bearing base-metal sulfide and invisible gold mineralization at Gabal Abu Houdied area, South Eastern Desert, Egypt. *Arabian Journal of Geosciences 8 (7)*, 4983–4997. https://doi.org/10.1007/s12517-014-1563-z

Ibrahim, W.S., Watanabe, K., Yonezu, K. 2016. Structural and litho-tectonic controls on Neoproterozoic base

metal sulfide and gold mineralization in North Hamisana shear zone, South Eastern Desert, Egypt: The integrated field, structural, Landsat 7 ETM+ and ASTER data approach. *Ore Geology Reviews 79 (62–77).* https://doi.org/10.1016/j.oregeorev.2016.05.012

Kabete, J.M, Groves, D.I., McNaughton, N.J., Mruma, A.H. 2008. A new tectonic subdivision of the Archean Craton of Tanzania and its significance to gold metallogeny. *Extended Abstract Volume, SEG-GSSA 2008.*

Kamihanda, G., Mushi, D., Ngerezi, M., Nyimbo, M., Balambirwa, O., Chakutema, B., Ramadhani, H. 2018. Report on Geological Investigation at Nholi Gold Rush, Dodoma. *Geological Survey of Tanzania internal report — unpublished.*

Kwelwa, S.D. 2017. Geological controls on gold mineralization in the Kukuluma Terrain. Geita Greenstone Belt, NW Tanzania. Doctoral dissertation Thesis, James Cook University. http://researchonline.jcu.edu.au/49987/

Leger, C., Barth, A., Falk, D., Mruma, A.H., Magigita, M., Boniface, N., Manya, S., Kagya, M., Stanek, K.P. 2015. *Explanatory notes for the minerogenic map of Tanzania. Geological Survey of Tanzania (GST).* Dar-es-Salaam, United Republic of Tanzania.

Liu, L., Zhou, J., Han, L., Xu, X. 2017. Mineral mapping and ore prospecting using Landsat TM and Hyperion data, Wushitala, Xinjiang, northwestern China. *Ore Geology Reviews 81*, 280–295. https://doi.org/10.1016/j.oregeorev.2016.10.007

Mars, J.C., Rowan, L.C. 2006. Regional mapping of phyllic- and argillic-altered rocks in the Zagros magmatic arc, Iran, using Advanced Spaceborne Thermal Emission and Reflection Radiometer (ASTER) data and logical operator algorithms. *Geosphere 2 (3)*, 161–186. *https://doi.org/10.1130/GES00044.1*

Masoumi, M., Honarmand, M., Salimi, A. 2021. Integration of concentration-area fractal model and relative absorption band depth method for mapping hydrothermal alterations using ASTER data. *Remote Sensing Applications: Society and Environment 23*, 100519. https://doi.org/10.1016/j.rsase.2021.100519

Matthew, M.W., Adler-Golden, S.M., Berk, A., Richtsmeier, S.C., Levine, R.Y., Bernstein, L.S., Acharya, P.K., Anderson, G.P., Felde, G.W., Hoke, M.P., Ratkowski, A., Burke, H.-H., Kaiser, R.D., Miller, D.P. 2000. Status of Atmospheric Correction Using a MODTRAN4-based Algorithm. *SPIE Proceedings, Algorithms for Multispectral, Hyperspectral, and Ultraspectral Imagery VI 4049*, 199–207. https://doi.org/10.1117/12.410341

Mbianya, G.N., Ngnotue, T., Wambo, J.D.T., Ganno, S., Pour, A.B., Kenne, P.A., Fossi, D.H., Wolf, I.D. 2021. Remote Sensing Satellite-Based Structural/Alteration Mapping for Gold Exploration in the Ketté Goldfield, Eastern Cameroon. *Journal of African Earth Sciences 184*, Article ID: 104386. https://doi.org/10.1016/j.jafrearsci.2021.104386

Mohamed, M.T.A., Al-Naimi, L.S., Mgbeojedo, T.I., Agoha, C.C. 2021. Geological mapping and mineral prospectivity using remote sensing and GIS in parts of Hamissana, Northeast Sudan. *Journal of Petroleum Exploration and Production 11 (3)*, 1123–1138. https://doi.org/10.1007/s13202-021-01115-3

Peyghambari, S., Zhang, Y. 2021. Hyperspectral remote sensing in lithological mapping, mineral exploration, and environmental geology: an updated review. *Journal of Applied Remote Sensing 15 (3)*, 031501. https://doi.org/10.1117/1.JRS.15.031501

Phillips, G.N., Powell, R. 2010. Formation of gold deposits: a metamorphic devolatilization model. *Journal of Metamorphic geology 28 (6)*, 689–718. https://doi.org/10.1111/j.1525-1314.2010.00887.x

Pinna, P., Muhongo, S., Mcharo, B.A., Le Goff, E., Deschamps, Y., Ralay, F., Milesi, J.P. 2004. *Geology and Mineral map of Tanzania Scale 1: 2,000,000.* Bureau deReserches Geologique et Minieres, University of Dar-es-Salaam, Geological Survey of Tanzania.

Pour, A.B., Hashim, M. 2011. Identification of hydrothermal alteration minerals for exploring of porphyry copper deposit using ASTER data, SE Iran. *Journal of Asian Earth Sciences 42 (6)*, 1309–1323. https://doi.org/10.1016/j.jseaes.2011.07.017

Pour, A.B., Hashim, M. 2014. ASTER, ALI and Hyperion sensors data for lithological mapping and ore minerals exploration. *Springer Plus 3 (1)*, 1–19. https://doi.org/10.1186/2193-1801-3-130

Pournamdari, M., Hashim, M., Pour, A.B. 2014. Application of ASTER and Landsat TM Data for Geological Mapping of Esfandagheh Ophiolite Complex, Southern Iran. *Resource Geology 64 (3)*, 233–246. https://doi.org/10.1111/rge.12038

Rowan, L.C., Schmidt, R.G., Mars, J.C. 2006. Distribution of hydrothermally altered rocks in the Reko Diq, Pakistan mineralized area based on spectral analysis of ASTER data. *Remote Sensing of Environment 104 (1)*, 74–87. https://doi.org/10.1016/j.rse.2006.05.014

Saadi, N.M., Watanabe, K. 2008. Lineaments extraction and analysis in Eljufra area, Libya. *Journal of Applied Remote Sensing 2 (1)*, 023538. https://doi.org/10.1117/1.2994727

Salem, S.M., El Sharkawi, M., El-Alfy, Z., Soliman, N.M., Ahmed, S.E. 2016. Exploration of gold occurrences in alteration zones at Dungash district, Southeastern Desert of Egypt using ASTER data and geochemical analyses. *Journal of African Earth Science 117*, 389–400. https://doi.org/10.1016/j.jafrearsci.2016.01.030

Schowengerdt, R.A. 2007. *Remote Sensing: Models and Methods for Image Processing*, 3rd ed. London: Academic Press.

Silverman, B.W. 1986. *Density Estimation for Statistics and Data Analysis*. London: Chapman and Hall.

Singh, A.K., Parkash, B., Choudhury, P.R. 2007. Integrated use of SRM, Landsat ETM+ data and 3D perspective views to identify the tectonic geo-

morphology of Dehradun valley, India. *International Journal of Remote Sensing 28*, 2403–2414. https://doi.org/10.1080/01431160600993397

Smith, M.J., Wise, S.M. 2007. Problems of bias in mapping linear landforms from satellite imagery. *International Journal of Applied Earth Observation and Geoinformation 9*, 65–78. https://doi.org/10.1016/j.jag.2006.07.002

Soulakellis, N.A., Novak, I.D., Zouros, N., Lowman, P.D., Yates, J. 2006. Fusing Landsat-5/TM imagery and shaded relief maps in tectonic and geomorphic mapping: Lesvos Island, Greece. *Photogrammetric Engineering and Remote Sensing 72*, 693–700. https://doi.org/10.14358/PERS.72.6.693

Testa, F.J., Villanueva, C., Cooke, D.R., Zhang, L. 2018. Lithological and hydrothermal alteration mapping of epithermal, porphyry and tourmaline breccia districts in the argentine andes using ASTER imagery. *Remote Sensing 10 (2)*, 203. https://doi.org/10.3390/rs10020203